Nanoalloy catalysts for electrochemical energy conversion and storage reactions

Shiyao Shan,[a] Jin Luo,[a] Jinfang Wu,[a] Ning Kang,[a] Wei Zhao,[a] Hannah Cronk,[a] Yinguang Zhao,[a] Pharrah Joseph,[a] Valeri Petkov[b] and Chuan-Jian Zhong*[a]

A key challenge to the exploration of electrochemical energy conversion and storage is the ability to engineer the catalyst with low cost, high activity and high stability. Existing catalysts often contain a high percentage of noble metals such as Pt and Pd. One important approach to this challenge involves alloying noble metals with other transition metals in the form of a nanoalloy, which promises not only significant reduction of noble metals in the catalyst but also enhanced catalytic activity and stability in comparison with traditional approaches. In this article, some of the recent insights into the structural and electrocatalytic properties of nanoalloy catalysts in which Pt is alloyed with a second and/or third transition metal (M/M′ = Co, Fe, V, Ni, Ir, etc.), for electrocatalytic oxygen reduction reaction and ethanol oxidation reaction in fuel cells, and oxygen reduction and evolution reactions in rechargeable lithium-air batteries are highlighted. The correlation of the electrocatalytic properties of nanoalloys in these systems with the atomic-scale chemical/structural ordering in the nanoalloy is an important focal point of the investigations, which has significant implications for the design of low-cost, active, and durable catalysts for sustainable energy production and conversion reactions.

[a]Department of Chemistry, State University of New York at Binghamton, Binghamton, NY, 13902, USA. E-mail: cjzhong@binghamton.edu

[b]Department of Physics, Central Michigan University, Mt. Pleasant, Michigan 48859, USA

1. Introduction

Significant advances in research and development have been made recently in harnessing the catalytic properties of nanoparticles on the energy and environmental fronts.[1–4] One important front involves a global search for sustainable and green energy, especially sustainable energy production, conversion, and storage, which are not only environmentally

Mr Shiyao Shan received his BS degree in Chemistry from Hunan University in 2010. He is currently pursuing his Ph.D degree in Chemistry at State University of New York at Binghamton under the guidance of Prof. Chuan-Jian Zhong. His current research focuses on synthesis, processing and characterizations of nanoalloy particles for sustainable energy conversion and storage. He has published more than 20 peer-reviewed articles, focusing on the structure–activity relationships in supported nanoalloy catalysts for various catalytic reactions, one of which is recently featured in Spotlights of Journal American Chemical Society.

Dr Jin Luo is a senior scientist in the Department of Chemistry at State University of New York at Binghamton, and an entrepreneur in NSC Technology and FlexSurface, Inc. His research interest involves interfacial electrochemistry, catalysis, sensors, and nanoscale chemistry. Currently his research focuses on developing advanced nanomaterials on rigid and flexible platforms for applications in fuel cells, batteries, chemical sensors, and biomedical devices. He is also leading R&D efforts in bringing some of the technologies to the market. He has co-authored more than 100 publications on these subject areas, and is co-inventor of a number of US Patents.
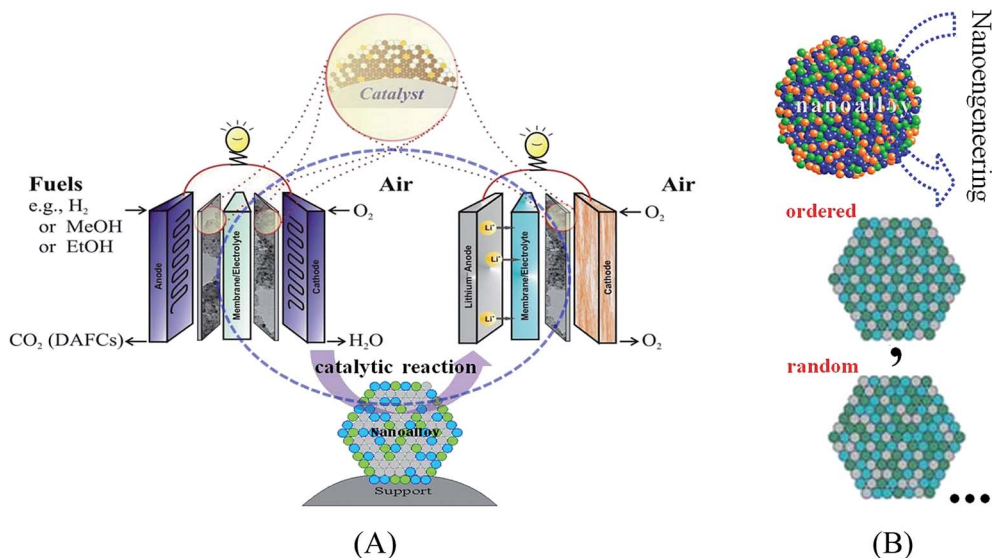
Fig. 1 (A) development of catalysts for electrochemical energy conversion and storage and (B) schematic illustrations of nanoalloys in terms of mixing patterns for ternary systems: ordered or random alloy structures.

cleaner but also more efficient than conventional fuels. To this end, one of the biggest challenges is the development of active, robust, low-cost catalysts, which is the key to electrochemical energy conversion and storage such as fuel cells and rechargeable lithium-air batteries (Fig. 1A). The design of nanoalloy catalysts with controllable sizes, shapes, compositions and structures is an important pathway towards active, robust, low-cost catalysts. In contrast to alloy which is a mixture of two or more metallic species existing either in a complete solid solution state with a single-phase, partial or phase-segregated state, nanoalloy differs from bulk alloys in several significant aspects in terms of mixing patterns and geometric shapes.[5]

In comparison with homogenous mixing of metal atoms in a single-phase alloy, the degree of segregation, mixing and atomic

Dr Chuan-Jian Zhong, Professor of State University of New York at Binghamton, has many years research experience working on the design of nanostructured catalysts for sustainable energy production, conversion and storage (e.g., fuel cells, batteries, etc.), and functional nanoprobes, assemblies and flexible devices for molecular/biomolecular recognition, medical diagnostics and other applications. He received National Science Foundation Career Award and 3M Faculty Research Award. He is author of more than 200 peer-reviewed research articles, and inventor of more than 10 US patents, and has given over 150 invited talks at national/international conferences, universities, industries, and national laboratories.

ordering depend on a number of factors,[5] including relative strengths of homoatomic *vs.* heteroatomic bonds, surface energies of the component element, differences in atomic sizes, charge transfer between the different atomic species, and strength of binding to surface ligands or support materials (Fig. 1B). For electrochemical reaction systems such as fuel cells and lithium-air batteries, the dissolution of certain metal components in the alloy ("dealloying") in the presence of acidic electrolytes, often being referred as Pt-skin structure formation,[6–11] could be influenced strongly by the structural types of the nanoalloys in terms of structural ordering, disordering, phase state, or d-band structure, which has attracted a great deal of attention in electrocatalysis.

A fundamental aspect on electrocatalytic activity and stability of nanoalloys is related to the metal oxide formation.[12,13] It is hypothesized that the removal of O-containing intermediates (–O, –OH, –OOH) resulting from the O=O breaking on the Pt-bridge sites, that recovers the catalytically-active sites, is possibly more effective by alloying Pt with two different metal components (M and M′) than with a single metal component. In addition to the electronic states such as the d-band centers, geometric factors as well as Pt–Pt distance change with the composition, computation of the oxygen and hydroxyl adsorption energies have shown that there is an approximate linear trend in oxygen reduction activity *vs.* O or OH binding energy for a large number of different transition and noble metals.[13] The fundamental understanding is important for the exploration of nanoalloy catalysts in energy conversion and storage devices, which will be the focus of this article. Some recent insights into the nanostructural characteristics of nanoalloy catalysts will be highlighted for several types of reactions in fuel cells such as proton exchange membrane fuel cells (PEMFC) and direct alcohol fuel cells (DAFC), as well as in rechargeable lithium-air (Li-Air) batteries.

PEMFC has become attractive because of high conversion efficiency, low pollution, lightweight, high power density, and a wide range of applications from power sources in automobiles and space shuttles to power grids for buildings and factories. In PEMFC, the large overpotential for oxygen reduction reaction (ORR) at the cathode represents a loss of about 20% from the theoretical maximum efficiency for the hydrogen/air fuel cells. Effective catalysts are needed for the reduction of the large overpotentials. Currently, low activity, poor durability and high cost of the platinum-based anode and cathode catalysts in PEMFCs constitute some of the major barriers to the commercialization of fuel cells. The kinetic limitation of the oxygen reduction at cathode catalysts is another problem for fuel cells operating at low temperature (<100 °C) because the rate of breaking O=O bond to form water strongly depends on the degree of its interaction with adsorption sites of the catalyst. Many studies focused on understanding the mechanism of oxygen reduction on Pt–Fe, Pt–Ni, and Pt–Co,[14] including CO- or methanol-tolerant.[15] Bulk-melted PtBi, PtIn, and PtPb intermetallic phases[16] and Ru nanoparticles modified with Pt[17] showed some promises for fuel cell applications. There are many examples of studying Pt alloys with early transition metals such as Co, Ni, Fe, Cr, Mn, V, *etc.* as catalysts for ORR in PEMFCs.[18–20] Studies on single crystalline thin films recently revealed that the addition of an early transition metal to Pt could change the atomic scale structures (Pt–Pt bond distance and coordination number) and electronic structures of Pt.[21,22] The ORR catalytic activity of different alloys depend on the type and concentration of the second metal in the subsurface atomic layers,[23–26] and a combination of the alloy size, shape, and structures.[2,4]

Alcohol fuel cells, such as direct methanol fuel cell (DMFCs) and direct ethanol fuel cells (DEFCs), become attractive because of high conversion efficiency, low pollution, lightweight, high power density, and applications from small power supplies for electronic devices such as PCs, notebooks, and cellular phones. In a typical alcohol fuel cell, oxidation reaction of methanol (in DMFC) or ethanol (in DEFC) occurs at the anode, where oxygen reduction reaction occurs at the cathode. In DMFCs, the oxidation of methanol on a catalyst layer in the presence of water forms carbon dioxide. Protons (H$^+$) are transported across the proton exchange membrane (*e.g.*, Nafion) to the cathode where they react with oxygen to produce water. Electrons (6 electrons) are transported through an external circuit, providing power to the connected load. The thermodynamic potential is 1.21 V. Both the methanol oxidation reaction at the anode and the oxygen reduction reaction at the cathode are highly irreversible and thus there is a loss of about 0.2 V at the anode for DMFC under open-circuit conditions, and an enhanced loss of about 0.1 V at the oxygen electrode because of the crossover of methanol from the anode to the cathode.[27] In DEFCs, ethanol is used instead of the more toxic methanol. Ethanol is an attractive alternative to methanol. In comparison with methanol, ethanol is a hydrogen-rich liquid and it has a higher energy density (8.0 kW h kg^{-1}) compared to methanol (6.1 kW h kg^{-1}). While ethanol has a 33% higher energy density than methanol, and can be obtained from renewable resources like sugar cane, wheat, or corn, a key challenge is the design of catalysts that can

effectively cleave the C–C bond.[28,29] The exploration of such cathode catalysts for non-aqueous and rechargeable lithium-air batteries is a recent advent because such batteries promise a tenfold increase of energy capacities in comparison with current lithium ion batteries. The major challenges for the practically viable rechargeable lithium-oxygen battery include however the unacceptably high overpotentials for the discharge–charge processes and the difficulty of achieving an optimal balance between the discharge capacity and the capacity retention on 'discharge–charge' cycling at the cathode. State-of-the-art Li–oxygen batteries have a full cycle during the charge process (3–4 V) efficiency of only 60%, largely due to the large voltages. The need of a catalyst in the air cathode to reversibly reduce oxygen and re-oxidize the oxide species back to oxygen largely stems from addressing the large overpotentials in the discharge–charge reactions, *i.e.*, the ORR on discharge and the oxygen evolution reaction (OER) on charge. Unlike ORR at the cathode of a fuel cell, the complication of the deposition of LiO$_2$ in ORR on the catalyst and the re-oxidation of LiO$_2$ in OER poses a new challenge for the design of an effective catalyst. The enhancement of the discharge capacity depends on a combination of factors including the catalyst activity and the overall catalyst structure. Various catalysts have been found to play an important role in the performance characteristics.[30]

In this article, some of the recent studies aimed at gaining insights into the structural details of nanoalloy catalysts in ORR, Ethanol oxidation reaction (EOR), Methanol oxidation reaction (MOR), and OER reactions relevant to fuel cells and Li-air batteries are discussed. The focus on the structural characterization is largely because of the new structural insights gained in recent years using synchrotron X-ray techniques. In light of some extensive previous reviews on the alloy catalyst performance,[1–5,11] this article attempts to highlight new insights from the structural characterization of the nanoalloy catalysts while providing sufficient discussion on the catalyst performance.

2. Nanoalloycatalysts and structural characteristics

Synthesis and processing

The synthesis of molecularly-capped metal nanoparticles as building blocks for engineering the nanoscale catalytic materials takes advantage of diverse attributes, including monodispersity, processability, solubility, stability, and self-assembly capability in terms of size, shape, composition, and surface properties. Indeed, the preparation of nanoparticles capped in monolayers, polymers or dendrimers is rapidly emerging, demonstrating remarkable parallels to catalytic activities for supported nanoparticles.[31–35] One important approach involves core–shell type synthesis.[36–39] The core–shell type nanostructure can be broadly defined as core and shell of different matters in close interaction, including inorganic/organic and inorganic/inorganic combinations.[33,40–45] The synthesis of metal nanoparticles in the presence of organic capping agents to form encapsulated metal nanoparticles has demonstrated promises

for preparing nanocatalysts with controllable size, shape, composition and surface properties.[33,39,41–45] The strategy based on molecular encapsulation has been used for the synthesis of different binary and ternary nanoparticles under controlled reaction conditions, such as AuM (M = Cu, Ag, etc.), PdM, PtM, and PtMM′ (M,M′ = Ni, Co, Fe, V, Cu, etc.).[46–56] The synthesis of these nanoalloy particles is in contrast to traditional approaches to preparing supported nanoparticle catalysts, which involve co-precipitation, deposition-precipitation, ion-exchange, impregnation, successive reduction and calcination, etc.,[57–64] and often have limited ability to control the size and composition due to the propensity of aggregation.

A key strategy in our approaches to the preparation of nanocatalysts involves molecularly-mediated synthesis of the nanoparticles using wet chemical method and post-synthesis thermochemical processing under controlled temperatures and atmospheres (Fig. 2 bottom panel). The removal of the organic encapsulation from metal nanoparticles is also an important step in the catalyst preparation. Among different strategies,[65] thermochemical processing strategy has demonstrated not only effective needs in removing the encapsulation, but also in refining the nanostructural parameters. The combination of the molecular encapsulation based synthesis and thermochemical processing strategies thus involves a sequence of steps for the preparation of nanoalloy catalysts: (1) chemical synthesis of the metal nanocrystal cores capped with ligands, (2) assembly of the encapsulated nanoparticles on supporting materials (e.g., carbon powders, TiO_2 or SiO_2),[47,66–68] and (3) thermal treatment of the supported nanoparticles.[69–71]

To firmly establish the molecularly-engineered synthesis and thermochemically-controlled processing pathways for the preparation of nanoalloy catalysts, there is a clear need to understand whether alloying or phase-segregation in multimetallic nanoparticles is different from bulk scale materials, and how the catalytic activity and stability are influenced by size, composition, morphology, support and phases has been an important focus of the recent research activities. Among a series of binary and ternary alloy nanoparticles supported on carbon,[47,49,52,72] one example is shown in Fig. 2 for PtNiCo nanoparticles. The as-synthesized $Pt_{39}Ni_{22}Co_{39}$ nanoparticles are highly monodispersed with a good crystallinity with narrow size distribution.[47,72]

After the thermochemical processing which removes the capping molecules and refine the nanoparticle structure, the HAADF (high-angle annular dark field) image reveals high crystallinity and the Pt, Ni and Co metal distribution across the entirenanoparticle. For AuPt and PdCu nanoalloys,[48,56,73,74] these nanoparticles display crystalline characteristics and largely uniform distributions of the two metal components. In our recent studies,[69,73,74] carbon-supported AuPt nanoparticles have been shown to exhibit single-phase alloying characteristics but also a controllable degree of partial alloying or phase segregation depending on the thermochemical processing conditions. The fully alloyed AuPt nanoparticles have a uniform distribution of the two metals across the nanoparticles. The bimetallic nanoparticles are not only crystalline with highly-faceted surfaces, but also have a uniform distribution of Au and Pt. Nanoparticles of other compositions[8,73,74] have also exhibited similar morphological characteristics. Similar nanocrystalline features and relatively uniform bimetallic distribution have also been observed for PdCu nanoparticles,[56] revealing that the bimetallic nanoparticle is basically a uniform alloy across the entire nanoparticle. Some of the nanoalloy catalysts prepared by certain combinations of the molecular encapsulation based synthesis and the thermochemical processing strategies are discussed next in terms of the alloying or phase-segregation
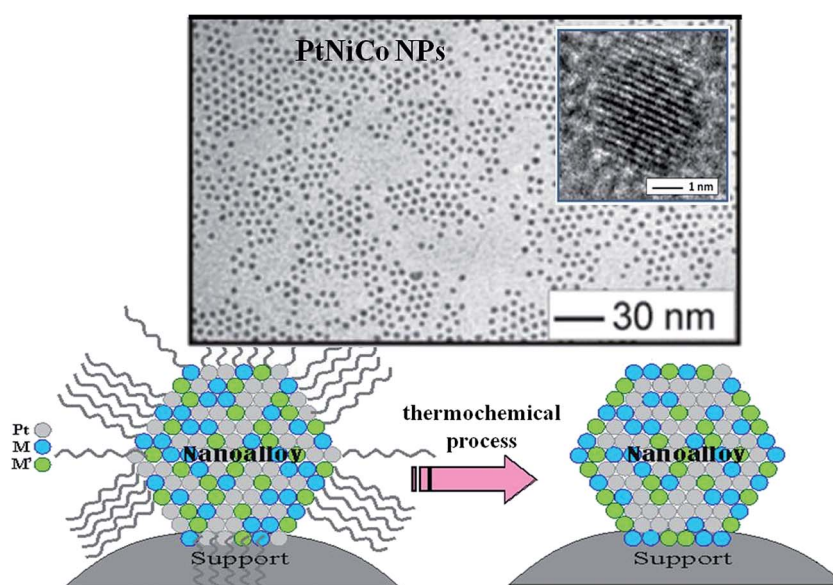

Fig. 2 A schematic illustration of molecularly-engineered synthesis and thermochemical processing of nanoalloy catalysts. Example TEM/HR-TEM images showing as-synthesized $Pt_{39}Ni_{22}Co_{39}$ nanoparticles (3.4 ± 0.4 nm). (Reproduced from ref. 72 with permission. Copyright 2012, American Chemical Society).

structures, focusing on the electrocatalytic reactions in correlation with the atomic-scale structural properties.

Structural characteristics

One of the key structural characteristics is the atomic-scale chemical and structural ordering of the nanoalloys in the thermochemically processed state, which is central to the exploration of the catalytic properties. Synchrotron X-ray techniques, including HE-XRD/PDFs and XAFS, have been demonstrated to be powerful for gaining insights into both extended and local atomic structures of nanoalloys. The HE-XRD/PDF study can be coupled with 3D simulations for determining the overall atomic-scale structure across the nanoalloy particle, including details of the chemical ordering. XANES/EXAFS is another powerful technique for determining the near neighbor metal–metal coordination, metal oxide content, electronic properties and charge transfer phenomena in the studied alloys in terms of local structural configurations. The combination of these two techniques provide information for short-range interatomic bonding and coordination structure about a specific atom as well as more extended structural/chemical ordering across the entire nanoparticle, regardless of whether the particle is crystalline or amorphous.[75,76]

For binary PtM and ternary PtMM′ (M/M′ = Co, Fe, V, Ni, *etc.*) supported on carbon, the manipulation of the thermochemical processing parameters can effectively refine the detailed atomic structures.[47,49,53] For example, $Pt_{39}Ni_{22}Co_{39}$/C catalyst, after the thermal treatment at different temperatures ranging from 400 to 926 °C, showed a single-phase alloy at all treatment temperatures.[77] However, a detailed analysis revealed a trend of lattice shrinking as the thermal treatment temperature is increased, showing a decrease of lattice constant from 0.385 nm for 400 °C to 0.377 nm for 926 °C. For $Pt_{45}V_{18}Co_{37}$/C catalyst,[49] the results revealed a gradual phase state transition from a random alloy fcc-type or chemically ordered alloy fct-type structure at 400 °C to chemically ordered fct structure at >400 °C where Pt, Co and V atoms are not randomly distributed within the nanoparticles but assume preferential ordering with respect to each other. The phase transition from a random alloy to a chemically ordered alloy type structure is often accompanied by a shrinking of the distances between the metal atoms.[78]

The HE-XRD/PDF results for PtIrCo/C, PtIr/C and PtCo/C catalysts treated from 400 and 800 °C (Fig. 3A and B) showed clear differences in crystallinity in terms of the sharpness of the peaks.[51] The PtIrCo catalyst at 400 °C are broad indicating a great structural disorder, and remains structurally quite disordered even when treated at 800 °C. The fcc-lattice model fits confirm the single phase state for the nanocatalysts. A shrinking of the lattice parameter from 3.797 to 3.737 Å is observed with increasing the temperature for PtIrCo catalysts, and from 3.874 at 400 °C to 3.867 Å at 800 °C for PtCo/C.[72,79,80] In contrast, the fcc-lattice parameter is found to increase from 3.877 to 3.880 Å with the temperature of treatment for PtIr/C. By closely examining the low-r part of the atomic PDFs, there is a clear evolution of the first-neighbor metal–metal distances with the temperature, showing first-neighbor metal–metal distance shrinking for

the case of PtIrCo and PtCo and expansion in the case of PtIr. The first neighbor metal–metal bond distances in the ternary catalyst are also shown to be considerably shorter than those in the binary ones.

The high-energy XRD experiments were also used to guide the Reverse Monte Carlo (RMC) simulations, as shown in Fig. 3C for a representative of snap shots of the atomic configurations. Each of the configurations has the real stoichiometry and size of the nanoalloy and atomic PDFs computed from the configurations match the experimental PDF data very well. $Pt_{45}Ir_{55}$ catalyst treated at 400 °C is a random alloy of Pt and Ir whereas that at 800 °C tends to segregate into a structure with Ir core and Pt enriched surface. This finding is qualitatively in agreement with the XPS based analysis of the relative surface composition, which showed a 16% increase in Pt upon treatment at 800 °C. $Pt_{73}Co_{27}$ catalyst treated at 400 °C features an alloy where Co atoms show some preference to the center of the nanoparticles whereas that at 800 °C, features an alloy with Co atoms being somewhat closer to surface of the particle. In comparison, the $Pt_{25}Ir_{20}Co_{55}$ catalyst treated at 400 °C features an alloy where Co and Ir species tend to occupy the inner part of the nanoparticles while Pt atoms show some preference to the surface of the nanoparticles. The ternary catalyst treated at 800 °C features a rather random type of alloy where Co, Pt and Ir atoms are almost uniformly distributed across the nanoparticles, a finding that was qualitatively in agreement with the small changes derived from the XPS analysis of the relative surface composition. These results reveal that the atomic distribution across the nanoparticles depends strongly on the binary/ternary composition and the thermochemical treatment temperature.

Another interesting example demonstrating the power of HE-XRD/PDFs in gaining atomic-scale insights into the nanoalloy structure is the AuPt nanoparticle system.[48] AuPt nanoalloys are analyzed using element-specific resonant HE-XRD technique. Both HE-XRD coupled with atomic PDFs (Fig. 4) and computer simulations prove the formation of Pt–Au alloys in particles less than 10 nm in size.

The bonding lengths in the alloys differing in 0.1 Å leads to extra structural distortion as compared to pure Pt and Au particles. In the nanoalloys, Au–Au and Pt–Pt bond lengths differing by 0.1 Å are revealed. The results demonstrate the presence of extra structural distortions for AuPt nanoparticles as compared to pure Pt and Au nanoparticles. Pt–Pt and Pt–Au pairs were identified in the first coordination shell of Pt atoms, providing atomic-scale insights into the alloy characteristic for the AuPt nanoparticles. RMC refined models are also used to aid the analysis of the alloy structures. Pure Au and Pt nanoparticles are used to produce model configurations for Au_mPt_{100-m} nanoparticles where Au and Pt atoms show various patterns of chemical order–disorder effects. All peaks in the partial Au–Au PDFs for Au_mPt_{100-m} nanoparticles are with largely diminished areas corresponding to reduced Au–Au coordination numbers that are characteristic of random type Pt–Au alloys. The alloying of Pt and Au occurs not only within a wide range of Pt–Au concentrations but is also stable in nanoparticles of different sizes. Importantly, the alloying characteristics of the less than 5
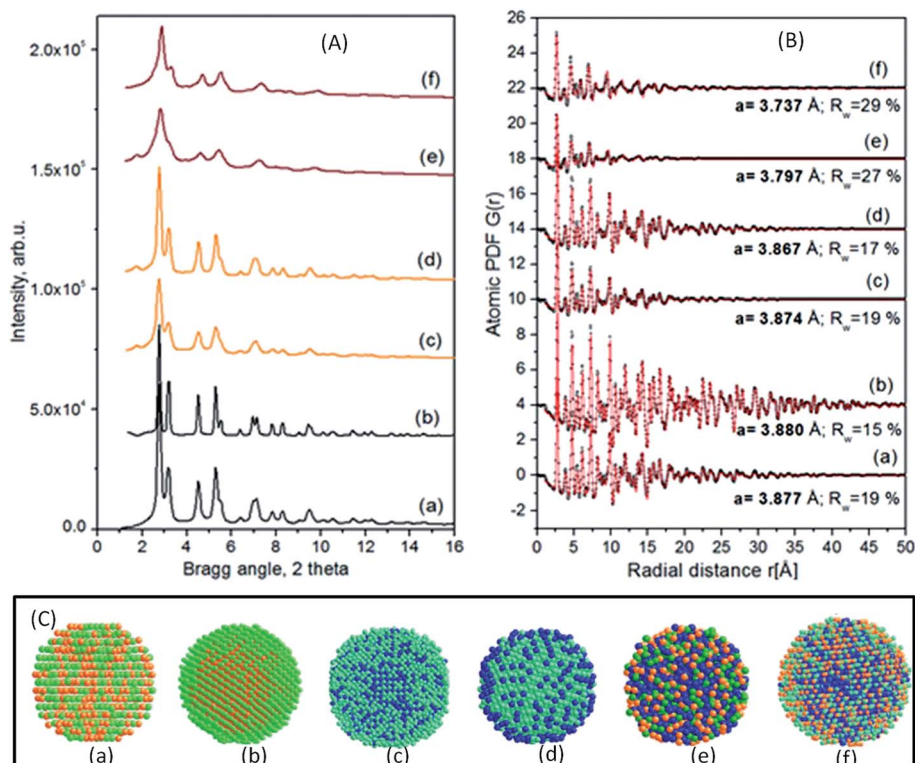
Fig. 3 (A) HR-XRD (λ = 0.1080 Å) experimental patterns for $Pt_{45}Ir_{55}$/C (a and b), $Pt_{73}Co_{27}$/C (c and d) and $Pt_{25}Ir_{20}Co_{55}$/C (e and f)treated at 400 (a, c, e) and 800 °C (b, d, f). (B) FCC-lattice constrained model fits (lines in red) to the experimental (symbols) atomic PDFs. The goodness-of-fit factors, R_w, and the refined fcc lattice parameters, a, are shown by each data set. (C) RMC (Reverse Monte Carlo simulation) constructed models for $Pt_{45}Ir_{55}$, $Pt_{73}Co_{27}$, and $Pt_{25}Ir_{20}Co_{55}$ processed at 400 °C. (Pt atoms: green, Ir atoms: orange, and Co atoms: blue). Note that the sizes of atoms are drawn not to scale to fit in the picture frame. (Reproduced from ref. 51 with permission. Copyright 2013, American Chemical Society).

nm sized AuPt particles were found to remain unchanged for a long period of time under ambient conditions, demonstrating structural stability of the nanoalloy.

The nanoscale alloying or phase segregation are also found to depend on the composition, support, and thermal treatment temperature for the supported Au_mPt_{100-m} nanoparticles.[69,73,74] There are currently two aspects of the fundamental insights that
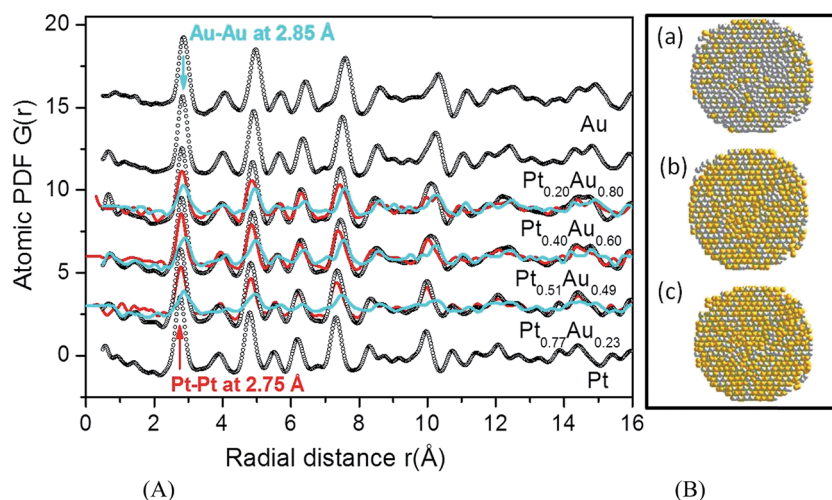

Fig. 4 (A) Low-r part of the experimental atomic PDFs for 5.1 nm Au–Pt particles (symbols). Experimental Pt–Pt differential PDFs (line in red) and Au–Au partial PDFs (line in cyan) are also shown. Arrows mark the positions of the Pt–Pt and Au–Au bond distances. (B) Cross sections of 5.1 nm Pt–Au particles (about 5000 atoms) with random alloy structure: (a) $Pt_{0.77}Au_{0.33}$; (b) $Pt_{0.51}Au_{0.49}$ and (c) $Pt_{0.40}Au_{0.60}$. Pt atoms are in gray, Au in yellow. (Reproduced from ref. 48 with permission. Copyright 2012, American Chemical Society).

are considered in supporting some of these alloying or phase-segregation states. One involves the theoretical finding of a negative heat of formation for AuPt nanoparticles smaller than ~6 nm, which constituted as a thermodynamic basis for favoring the formation of alloyed phase.[81] The other involves the theoretical finding of a possible phase segregation of AuPt particles as a result of the combination of larger surface free energy of Pt (2.48 J m^{-2}) than Au (1.50 J m^{-2})[81] and the lower melting point of smaller-sized nanoparticles than larger-sized particles ($T \propto 1/r_{(particle\ radius)}$).[82] The nanoscale phase of Au_mPt_{100-m} nanoparticles is a very important parameter for the exploration of the nanoscale bimetallic functional properties. The lattice constants of the bimetallic nanoparticles were found not only to scale linearly with Pt%, in contrast to the bulk AuPt counterparts which display a miscibility gap at 20–90% Au, but also to be smaller than those of the bulk counterparts.[73,83] This finding was the first example demonstrating that the nanoscale AuPt nanoparticles could exhibit single-phase character and reduced inter-atomic distances in the entire bimetallic composition range in contrast to with the bulk counterparts.[73,83] In addition to the latest HE-XRD/PDFs evidence,[48] results from theoretical modeling and Density Functional Theory (DFT) computation for small AuPt nanoparticles (~1.2 nm) has also revealed a difference in the lattice constant – composition relationship between the nanoscale and the bulk systems in agreement with the experimental data.[73,74] In theoretical modeling of realistic particle sizes, a negative heat is revealed for the formation for AuPt particles smaller than ~6 nm,[81] thermodynamically favoring the formation of alloyed phase. The atomic distributions of Au and Pt are also shown to change in distance from the center of mass in the nanoparticle depending on temperature and support.[84] The complex phase properties are also supported by *in situ* time-resolved X-ray diffraction study of phase change kinetics at high temperature.[85] The nanoscale phase evolution has a significant impact on the surface alloying or segregation,[69,83,86] as supported by FTIR probing of CO adsorption as a function of the bimetallic compositon[83] and XPS analysis of the relative surface composition as a function of the treatment temperature.[69,74]

DFT computation of small AuPt nanoparticles (~1.2 nm) has provided some insights into the phase properties.[74] Seventeen 55-atom AuPt nanoparticles (~1.2 nm), including six $Au_{24}Pt_{76}$ (13 Au atoms and 42 Pt atoms), five $Au_{49}Pt_{51}$ (27 Au atoms and 28 Pt atoms), and six $Au_{76}Pt_{24}$ (42 Au atoms and 13 Pt atoms) were studied using DFT calculations. These calculations were carried out using the spin-polarized DFT method that is implemented in Vienna Ab initio Simulation Package (VASP).[81,87,88]

The stability of alloy structures was found to lie in between the core–shell structures. The complete Pt-core/Au-shell structure is the most stable among all isomers. The least stable isomer has the least number of surface Au atoms. When temperature increases, the alloy nanoparticles evolve in such a way that the outer shell Pt atoms migrate into the inner shell. This is further supported by molecular dynamics simulations,[89] where upon heating above 600 K such Pt migration takes place in an alloy nanoparticle of ~3.6 nm. The computational results

further indicate that thermal treatments of alloy AuPt nanoparticles should be below certain temperatures to prevent the loss of outershell Pt atoms. DFT-calculated lattice constants are indeed smaller than that of bulk. This finding is in agreement with our earlier finding of the nanoscale phase properties for the alloyed AuPt/C catalysts.[90] The computation results supported the observed overall lattice shrinking of the metal and bimetallic nanoparticles in comparison with the bulk counterparts, and showed the possibility of an evolution of the alloy nanoparticles in such a way that the outer shell Pt atoms migrate into the inner shell when temperature increases, which is qualitatively consistent with the XRD analysis results. There are many recent examples on DFT computational modeling of AuPt nanoparticle structures in terms of composition and structures[91] For example,[91] the study of AuPt nanoalloys with 55 atoms with an intermediate composition range by a procedure combining global optimization searches within an atomistic potential model with DFT relaxation of the lowest-energy isomers identified two structural motifs in close competition: the Mackay icosahedrons and an asymmetric capped decahedron.

3. Electrocatalytic properties of nanoalloys

While significant progress has been made in the research and development of various catalysts for the electrochemical energy conversion and storage devices, challenges remain especially in atomic-scale structural understanding of alloy catalysts in correlation with their catalytic properties. Some recent results in our investigations of nanoengineered alloy catalysts for oxygen reduction reaction in PEMFCs, methanol or ethanol oxidation reactions involved in DMFCs or DEFCs, and oxygen reduction and evolution reactions at the air cathode in Li-air batteries are discussed. The nanoalloys, depending on the composition and structures, exhibit interesting synergies for electrocatalytic ORR, MOR, OER, which are highlighted in the next two subsections.

Electrocatalytic oxygen reduction reaction

A fuel cell is an electrochemical energy conversion device that converts hydrogen at the anode and oxygen at the cathode through a membrane electrode assembly (MEA) into water and produce electricity. For ORR at the cathode of a PEMFC, the desired reaction pathway is 4e$^-$ reduction reaction, but the voltage is in general the summation of the thermodynamic potential E_{Nernst}, the activation overpotential η_{act} (from both anode and cathode overpotentials, *i.e.*, $\eta_{act(cathode)} - \eta_{act(anode)}$), and the ohmic overpotential η_{ohmic}. While the thermodynamic potential is governed by Nernst equation in terms of the E_0 (1.23 V) and the operating concentrations (P(H$_2$) and P(O$_2$)), the activation overpotential is dependent on the electrode kinetics in terms of current flow, and the overpotentials associated with catalyst activity ($\eta_{act(catalyst)}$). The overpotential $\eta_{act(catalyst)}$ is large mainly due to the sluggish activity of ORR. The adsorption of O$_2$ could produce Pt–O or Pt–OH in a dissociative adsorption

which constitutes a 4 electron reduction pathway forming water, or Pt–O_2^- or Pt–O_2H in an associative adsorption which often proceeds in a 2 electron reduction pathway forming hydrogen peroxide. While concepts based on Pt skin on an alloy or dealloyed surface can explain partially some of the experimental facts, the understanding of how Pt–O or –OH intermediate species could influence the overall ORR because their binding strength and the formation and removal of Pt–O/Pt–OH species are known to play an important role in the overall electrocatalytic ORR over Pt-alloy catalysts. The rational design of Pt-alloys involving transition metals (M/M′) could create a bifunctional (or multifunctional) synergy for the formation and removal of Pt–O or Pt–OH species. For ternary catalyst, the introduction of a second M′ into Pt-M alloy may lead to a manipulation of the surface oxophilicity by maneuvering –O/–OH species over M and M′ sites through structural or compositional effect. The understanding of how Pt–OH and Pt–O binding energies can be tuned by the M/M′ oxophilicity would aid the design of the alloying metals for synergistic formation and removal of Pt–OH species in correlation with the structural and chemical complexity of the nanoalloys.[75,76]

The kinetic current (i_k)[92] is used to determine the mass activity (MA, current density per unit mass of Pt) and specific activity (SA, current density per unit area of Pt). To obtain the MA and SA, the kinetic current is usually extracted from the RDE without IR-drop correction,[49,51,85,93] or after a correction of IR drop in the RDE curves.[94,95] The "IR-drop"-corrected mass activity is typically higher than that without IR-drop correction.[96] For ternary nanoalloy PtNiCo, the RDE measurement of the kinetic current without IR correction.[77] shows a major enhancement in electrocatalytic activity for ORR in comparison with pure Pt and the bimetallic nanoalloy counterparts. In the case of $Pt_{36}Ni_{15}Co_{49}$/C catalysts after thermochemical treatment, there is a clear indication of the kinetic current increase with increasing the thermochemical treatment temperature (Fig. 5a).[77] By further comparing the mass activity and the specific activity as function of the treatment temperature, there is a clear trend showing the increase of both mass and specific activities with increasing the treatment temperature, reaching a

plateau at 800 °C (Fig. 5b). The mass activity of $Pt_{36}Ni_{15}Co_{49}$/C treated at 800 and 926 °C is more than four times higher than that of commercial Pt/C. The increased electrocatalytic activity is associated with the interatomic distance shrinking in the nanoalloy with increase of the thermochemical treatment temperature.

A maximum activity is revealed for $Pt_{45}V_{18}Co_{37}$/C catalyst treated under oxygen followed by reduction by hydrogen ("O + H" treatment) as a function the thermochemical treatment temperature (Fig. 6).[49] At temperatures from 400 to 700 °C, the mass activity and specific activity show a significant increase with the temperature in comparison with those for the commercial Pt/C catalyst and the $Pt_{45}V_{18}Co_{37}$/C catalysts treated under nitrogen followed by hydrogen reduction ("N + H" treatment) (Fig. 6b). The chemically ordered fct lattice model, however, becomes increasingly a better match to the experimental PDFs for the particles annealed at >400 °C. Upon increasing the annealing temperatures, the degree of the structural order increases, which is accompanied by the interatomic distance shrink and rearrangement of Pt and Co/V species in a chemically ordered fct type structure, leading to an enhanced catalytic activity for ORR. The further increase of the degree of chemical and structural ordering at annealing at temperatures higher than 600 °C has little or even detrimental effect on the activity enhancement, implying the existence of an optimal structure of the alloyed Pt sites for the adsorption and activation of molecular oxygen. In comparison to ORR activities of PtNiCo showing a gradual increase with temperature (Fig. 5), PtVCo shows a maximum at 600 °C (Fig. 6), which coincides with the temperature corresponding to the phase transition from fcc type to fct type.

The PDF data for $Pt_{45}V_{18}Co_{37}$/C[49] revealed a phase transition from a random alloy to a chemically ordered alloy type structure as the thermochemical treatment temperature increased, which is accompanied by a shrinking of the distances between the metal atoms, as discussed earlier. The trend in these structural features correlates well with the increase of MA and SA with the annealing temperature reaching a maximum at 600 °C. Above 600 °C, the subtle levelling off in the SA value and the slight
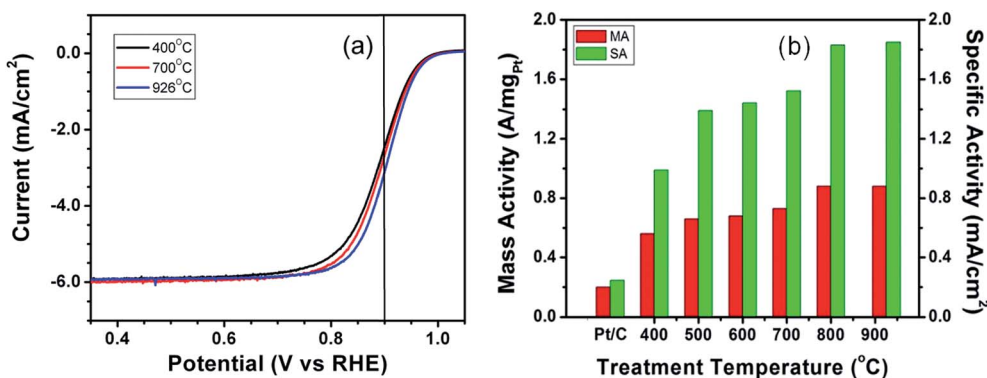

Fig. 5 RDE curves (a) and plots of mass activity (MA) (left, red) and specific activity (SA) (right, green) (b) at 0.900 V (vs. RHE) for a set of Pt_{36}-$Ni_{15}Co_{49}$/C catalysts treated at different temperatures. The result for a commercial Pt/C catalyst is included for comparison. (Reproduced from ref. 77 with permission. Copyright 2010, American Chemical Society).
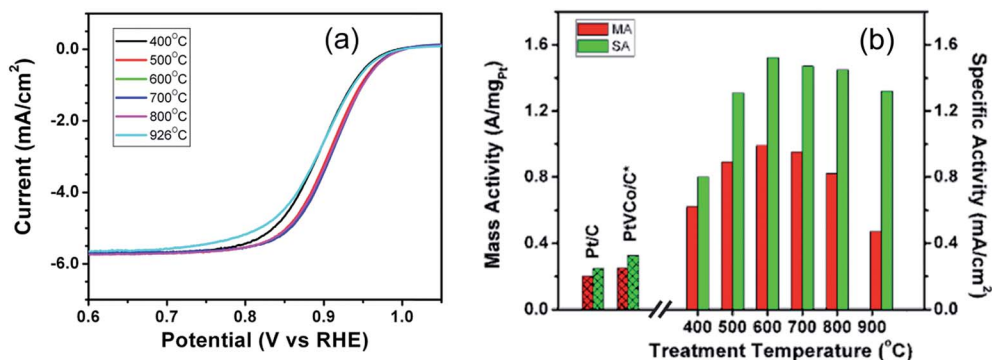
Fig. 6   RDE curves (a) and plots of mass activity (MA) (left, red) and specific activity (SA) (right, green) at 0.900 V (*vs.* RHE) for $Pt_{45}V_{18}Co_{37}/C$ after "O + H" treatment at different temperatures (Note that data for the catalyst treated by "N + H" at 400 °C (PtVCo/C*) and a commercial Pt/C catalyst are also included for comparison) (b) in O_2-saturated 0.1 M $HClO_4$. Pt loading = 6.6 ug cm^{-2}, scan rate: 10 mV s^{-1} at 1600 rpm, (reproduced from ref. 49 with permission. Copyright 2012, American Chemical Society).

drop in the MA value likely indicates that the further increase in the chemical ordering and shrinking in interatomic distances has little or even detrimental effect on the activity enhancement. This is understandable because the adsorption and activation of molecular oxygen requires an optimal structure of the alloyed Pt sites.

By analysing the data in the kinetic region (Fig. 7), the MA obtained for the ternary PtIrCo/C system is found to be ~2 times higher than those of two binary catalysts (PtCo/C and PtIr/C).[51] The substantially shorter metal–metal distances in the ternary nanocatalysts are believed to be responsible for the improved catalytic properties. The increase in SA from lower to higher temperature for the ternary nanoalloys is also likely due to the further decrease in the metal–metal distances and the changes in coordination numbers. In addition to a favorable change in Co–Pt first coordination number, there are also changes in Co–Ir, Pt–Ir and Ir–Ir coordination numbers indicating an increased degree of alloying. Moreover, the introduction of Ir in

PtCo to form a ternary system was indeed shown to increase stability of the electrocatalytic activity.[79] The fact that the PtIrCo catalysts still showed a higher stability than PtCo also indicates that the addition Ir played an important role in strengthening the stability.[79]

In comparison with the evolution from a random type of alloy at 400 °C to an Ir_core-Pt_enriched surface structure at 800 °C for PtIr, and from a structure with a Co rich core at 400 °C to a structure with a slightly Co-enriched surface at 800 °C for PtCo, there is distinctive evolution from alloy with Co–Ir core and Pt rich surface at 400 °C to an alloy where Co, Pt and Ir species are more uniformly distributed across the nanoparticles at 800 °C for the ternary PtIrCo (Fig. 3C). Both MA and SA are the highest for the ternary catalyst among the three catalysts. The 2× increase of specific activity for the ternary catalyst in comparison with the relatively small increase for PtIr indicates the importance of adding a third metal to the alloy. The marked enhancement of the activity ternary nanoparticles is believed to
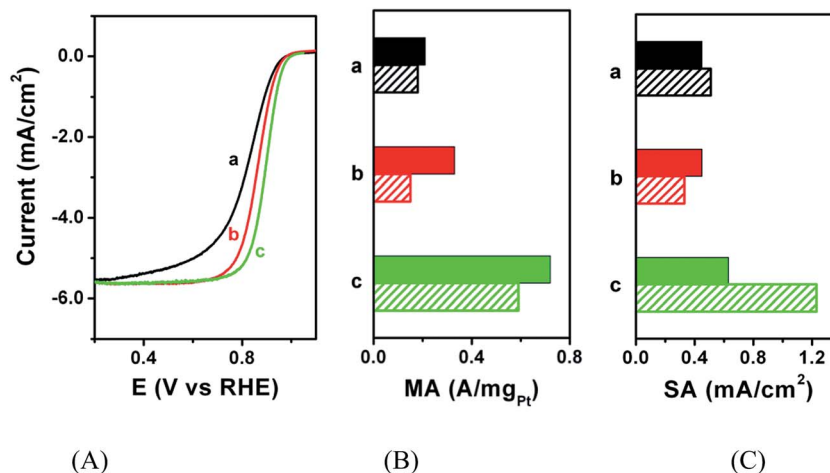

Fig. 7   Electrocatalytic activities for ORR in O_2-saturated 0.1 M $HClO_4$: RDE curves for 400 °C treated catalysts (A), and mass (MA) (B) and specific activities (SA) (C) for 400 (filled bars) and 800 °C treated catalysts (patterned bars) (C). Catalysts: $Pt_{45}Ir_{55}/C$ (a), $Pt_{73}Co_{27}/C$ (b), and $Pt_{25}Ir_{20}Co_{55}/C$ (c). Data for PtCo/C and PtNi/C with similar Pt content and commercial E-tek Pt/C are included for comparison. (Reproduced from ref. 51 with permission. Copyright 2013, American Chemical Society).

be linked to the decrease in the 1st Metal–Metal distances and the formation of alloy featuring either an Co–Ir core with Pt rich surface or a uniform distribution of Co, Pt &Ir species across the entire nanoparticle.

In comparison with commercial Pt catalyst, the mass/ specific activities for a series of Pt-ternary catalysts for ORR (extracted from RDE curves at 0.900 V in 0.1 M $HClO_4$ electrolyte without IR-drop correction), including PtNiCo/C, PtVCo/C, PtNiFe/C, PtIrCo/C, and PtVFe/C,[49,51,72,77,79,80,85] exhibit greatly enhanced mass activities and specific activities (Fig. 8). PtNiCo/ C and PtVCo/C catalysts exhibit the highest mass and specific activities. The enhancement of the activities for the ternary catalysts is also found to outperform the binary ones, as demonstrated for PtNiCo/C[72,77] with PtNi/C and PtCo/C.[80] The presence of subtle differences in redox potentials and metal lattices of the different base metals in the ternary alloy possibly allows better maneuvering of atoms in the nanoalloy formation and annealing processes than those in the binary counterparts.

The enhanced electrocatalytic activity for these ternary nanoalloys correlates with the atomic distances and phase state tunable by the transition metal components or the thermo-chemical processing parameters. For PtNiFe/C catalyst,[97] Pt–Pt bond distance was measured accurately by EXAFS, and no difference was observed. Qualitatively, the Pt sites on the surface are relatively richer for the catalyst treated at 400 °C than that at 800 °C, although they are less active for the former. Therefore, the lower-temperature treated catalyst is more active on a mass basis (*i.e.*, the number of active sizes dominates). On the other hand, the specific activity data from RDE revealed an opposite trend; that is, the catalyst treated at the higher temperature showed a higher activity than the catalyst treated at the lower temperature. The higher specific activity for the higher temperature treated catalyst reflects the likelihood of a better Pt alloying with Fe or Ni. The difference in the surface metal oxides and alloying structures between the catalyst treated at 800 °C with a larger particle size (7.8 nm) and the catalyst treated at 400 °C with a smaller particle size (5.3 nm), as revealed by XAFS analysis, has demonstrated the significant role

played by both particle size and surface atomic structure of the catalyst.

The understanding of this type of Pt-nanoalloy properties in terms of M or M′ is useful for creating a bifunctional or multi-functional synergy for effective maneuvering surface oxygenated species over the M/M′ sites through structural or compositional effect.

Electrocatalytic oxidation of alcohols

Some of the nanoalloy catalysts exhibit electrocatalytic activity for MOR and EOR. A key to the design of nanoalloy catalysts for MOR is the understanding of the catalytic synergy on the surface. MOR over AuPt catalysts serves as an interesting example of the operation of bifunctional catalytic synergy.[73] The design and control of spatial arrangement of Au and Pt in AuPt nanoparticles are critical for exploiting the nanoscale bifunc-tional catalytic activity where Pt provides a site for catalyzing methanol oxidation or oxygen reduction reactions and Au provides a site for adsorption of hydroxide groups or oxidation of CO to CO_2.[85,98,99] The understanding of the synergistic elec-trocatalytic activity of AuPt/C in MOR has been an important focus of interests in this bimetallic system.[83,100] For MOR, one of the most significant findings is that the mass activity in the alkaline electrolyte exhibits a maximum around 65–85% Au (Fig. 9A). Considering the modeling results for CO adsorption on small clusters of AuPt for CO adsorption, the Au atoms surrounding Pt atoms in the AuPt alloy are believed to have played an important role in either removing the intermediate CO-like species and/or providing oxygenated species in the methanol oxidation process (see Fig. 9B). This assessment is consistent with the known facts that the nanoscale Au is highly active for CO oxidation, and produces surface oxygenated species in basic electrolytes. A further analysis by using HE–XRD/PDF techniques[48] has demonstrated: (i) the unchanged Pt–Pt bond distances in nanoalloy for the adsorption of meth-anol on Pt–Pt sites for dehydrogenation; (ii) the unchanged Au–Au bond distances helps the adsorption or addition of hydroxyl groups to the intermediate CO species, and (iii) the presence of
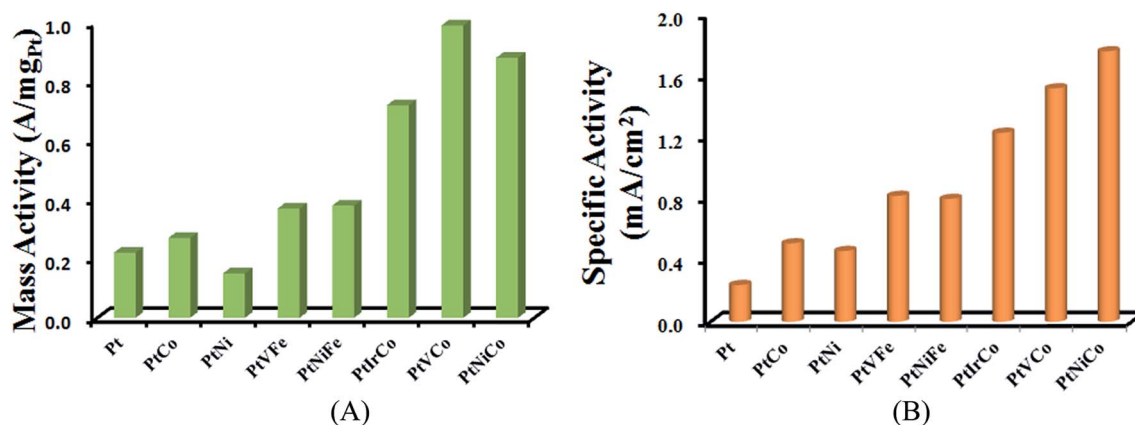

Fig. 8 Comparisons of ORR mass activities (A) and specific activities (B) at 0.9 V *vs.* RHE in 0.1 M $HClO_4$ for the Pt-binary including PtCo and PtNi[80] and Pt-ternary catalyst including PtNiCo,[72] PtVCo, PtNiFe, PtIrCo, PtVFe with commercial pure Pt/C. Note that the compositions of the nanoalloys chosen in the bar chart are those with about 50 atom% Pt for the comparison.
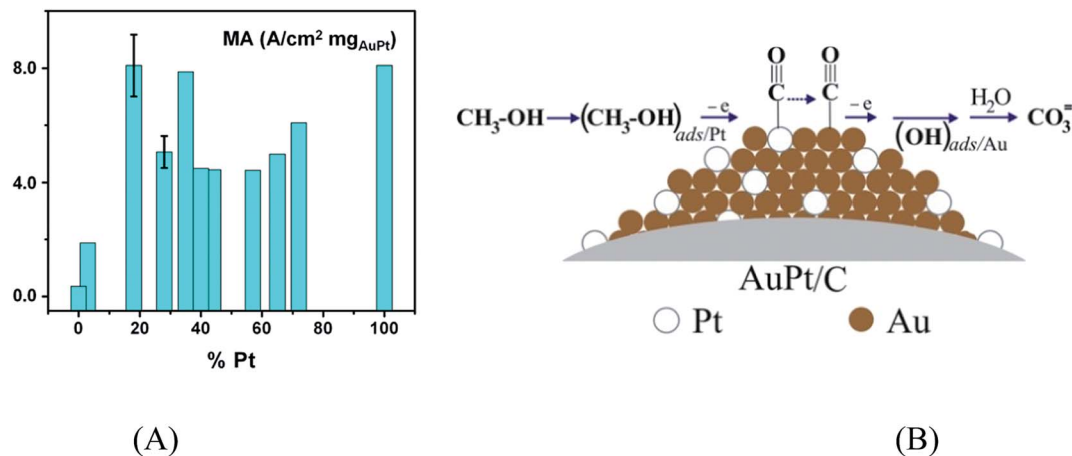
Fig. 9 (A) Plots of mass activity as a function of composition in alkaline electrolytes[48] (B) in terms of a surface adsorption and hydrogenation of methanol $(CH_3-OH)_{ads}$ on Pt sites, an intermediate reaction step of $C\equiv O$ transfer (marked with an arrow) from Pt to neighboring Au sites, and the addition of hydroxyl (OH) and water (H_2O) from the latter sites to the $C\equiv O$ species resulting in the formation of the final carbonate product $(CO_3^=)_{soln}$. (Reproduced from ref. 73 with permission. Copyright 2010, American Chemical Society).

Pt–Au sites facilitates the transfer of intermediate species from Pt and Au.

In terms of a relative Pt-specific mass activity for MOR in akaline solution, a maximum activity is observed at Au concentration of 60–80%. Note pure Au nanoparticles are not active for this reaction, and there is no apparent indication of size and shape effect,[101] and not change in Au–Au and Pt–Pt bond lengths.[102–104] Due to the difference in their electronegativity, mixing of Pt and Au atoms results in small but not negligible Pt-to-Au net charge transfer.[105–107] Such charge transfer will occur throughout the alloy nanoparticles modifying the electron density distribution of all atoms involved.[83,108–114] Note alloying throughout the nanoparticles is important since studies show that not only the very top nanoparticle's layer but at least 3 atomic layers close to the nanoparticle's surface influence the catalytic properties. With nanoparticles a few nm in size about 30–50% of the total numbers of atoms are in those layers. Due to the Pt-to-Au partial charge transfer there will be an increase of the d-band vacancy at the Pt sites that may facilitate the removal of intermediate CO-like species from them toward the neighboring Au sites greatly facilitating the formation of the carbonate $(CO_3^=)$ product of the oxidative dehydrogenation of methanol. This synergistic effect (Fig. 9) involves adsorption and hydrogenation of methanol (CH_3OH) on Pt sites, an intermediate step of transferring $C\equiv O$ from Pt sites to neighboring Au sites, and the addition of hydroxyl and water from the latter to $C\equiv O$ resulting in the formation of the final carbonate $CO_3=$ reaction product. The presence of Pt–Pt and Pt–Au pairs in the first coordination shell of Pt atoms, *i.e.* the complete alloying of Pt and Au, is believed to play an important role in this mechanism. In particular, the unchanged Pt–Pt bond distances in the alloy particles ensures the adsorptive dehydrogenation of methanol molecules that tend to line up with Pt–Pt bonds. On the other hand, the unchanged Au–Au bond distances help the adsorption and addition of hydroxyl groups to the intermediate CO-like species. In addition, the increased d-band vacancy on the Pt sites and respective electron enrichment on Au sites facilitates the transfer of those intermediate species from Pt sites to the neighboring Au sites.

For ethanol based fuel cells, one of the key problems is the need of highly effective catalysts, which is considered to be much more challenging than the study of catalysts for direct methanol fuel cells (DMFCs).[115,116] This is largely due to the difficulty in C–C bond cleavage for the complete oxidation of ethanol to CO_2. In addition to the extensively-studied platinum catalysts, palladium-based systems have received an increased interest. The mechanism of the ethanol oxidation reaction on Pd in alkaline media is believed to involve the removal of the adsorbed ethoxi by the adsorbed hydroxyl as the rate-determining step.[117,118] There is a much larger activation energy required for the oxidation of ethanol than methanol because the ability to reduce the activation energy for C–C bond determines how easier the bond cleavage is over a catalyst. Despite increasing demonstrations of the catalysts for ethanol oxidation, the understanding of the catalyst design and structures for achieving C–C cleavage of ethanol in its electro-oxidation remains elusive. Two examples demonstrating the C–C bond cleavage include oxidation of ethanol to CO_2 over Pt/Rh/SnO_2 electrocatalysts in an acidic electrolyte,[28] and in alkaline solutions containing Pb(IV) acetate as a co-catalyst of Pt electrode.[29] These studies have provided some useful information for the design of catalysts for achieving C–C bond cleavage.

The electrocatalytic activities for ethanol and methanol oxidation over PdCu/C catalysts are also compared (Fig. 10).[56] For MOR, the forward peak was at ~-0.19 V and backward peak was located at ~-0.37 V. The current intensity of forward peak was four times larger than backward peak. For PdCu/C for EOR, the forward peak was at ~-0.21 V and backward peak was located at ~-0.30 V. The current intensity of the backward peak was about two times larger than forward one. It is evident that the PdCu alloy catalyst showed a higher electrocatalytic activity
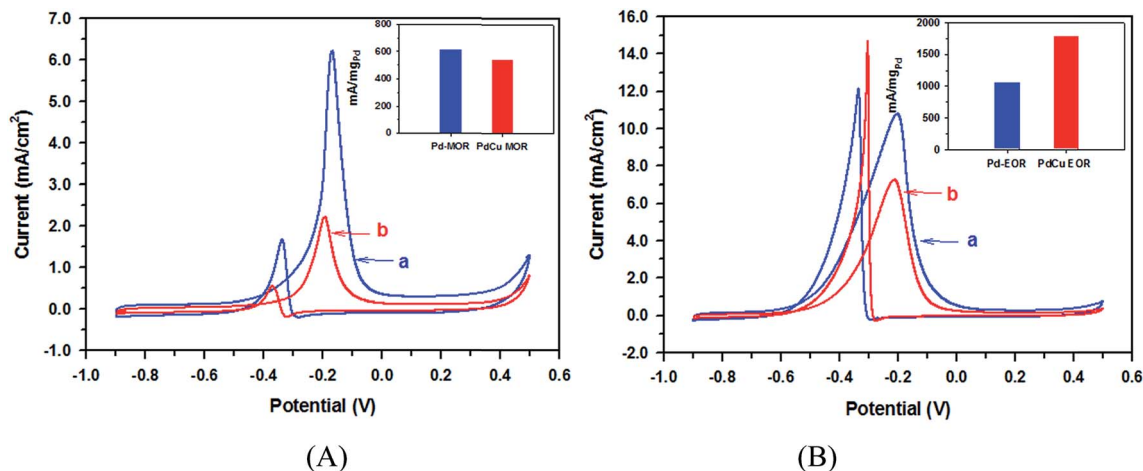
Fig. 10 Cyclic voltammetric curves for Pd/C (20%) and $Pd_{21}Cu_{79}$/C (40%), (on GC electrode, 0.196 cm^2) in 0.5 M KOH with 0.5 M methanol (A: Pd/C (a), $Pd_{21}Cu_{79}$/C (b)), and 0.5 M ethanol (B: Pd/C (a), $Pd_{21}Cu_{79}$/C (b)). Inserts: comparisons of mass activities. Scan rate: 20 mV s^{-1}. Reference electrode: Ag/AgCl with saturated KCl. (Reproduced from ref. 56 with permission. Copyright 2013, American Chemical Society).

than Pd/C for EOR, but a slightly lower activity for MOR. This finding is intriguing because the operation of the synergy as a result of the surface enrichment of Pd on the alloy.

CO_2 is detected as a product by analyzing the gas sample from the sealed top compartment of an electrolysis cell with PdCu/C catalyst supported on a high surface area vitreous carbon electrode. Almost no aldehyde is detected, but trace of CH_3COOH is detected. Since CH_3COOH is soluble in the acid-treated electrolyte, the detected trace of CH_3COOH in the gas phase is a fraction of the total CH_3COOH produced, suggesting CH_3COOH is part of the products. While quantitative aspects of the electrolysis data and the GC data are yet to be further delineated, the data did provide an indication for CO_2 product being released from the electrolysis, suggesting that the electrocatalytic oxidation involves C–C cleavage over the PdCu catalyst.

Nanoalloy catalysts in the air cathode of Li-air battery

In comparison with the long-standing problems in the development of catalysts for fuel cells, the study of catalysts for reactions involving electrochemical energy storage devices such as rechargeable Li-air batteries is a relatively recent advent.[30,119,120] Rechargeable Li-air batteries have attracted a great deal of interest because of their gravimetric theoretical energy density (1800–2800 W h kg$_{positive}^{-1}$) is much higher than regular Li-ion battery (600 W h kg$_{positive}^{-1}$).[30] While non-aqueous and rechargeable lithium-air batteries promise a 10-fold increase of energy capacities in comparison with current lithium ion batteries, major challenges for the practically-viable rechargeable lithium-oxygen battery include however the unacceptable high overpotentials for the discharge–charge processes and the difficulty to achieve an optimal balance between the discharge capacity and the capacity retention on "discharge–charge" cycling at the cathode. In the air cathode of a fuel cell system, e.g., PEMFC, the reaction product water is released from the cathode materials or catalysts. However, on

the cathode materials of a rechargeable lithium-air battery, the reaction product, e.g., lithium peroxide remains on the cathode materials. For the formation and re-oxidation of lithium peroxide on the cathode materials, the reversible cell voltage is 2.96 V with respect to the redox potential of Li/Li$^+$. To overcome the large overpotentials in the discharge–charge reactions, i.e., the ORR on discharge and the oxygen evolution reaction (OER) on charge, there is a need of a catalyst in the air cathode to reversibly reduce oxygen and re-oxidize the oxide species back to oxygen. At the cathode, the discharge reaction involves the formation of lithium peroxide (or superoxide as intermediate species) on the cathode materials. For reducing O_2 to O_2^- in a nonaqueous environment, the work by Abraham et al.[121] showed that the cations strongly influence the reduction mechanism. The study by Zhang et al.[122] demonstrated the importance of hydrophobicity and polarity of nanoaqueous electrolytes on the performance of Li-air batteries. Among the reported cathode materials,[123–126] manganese oxides are perhaps the most extensively studied and work the best in a lithium–oxygen battery in terms of energy capacity. For example, a Li–O_2 battery with a-MnO_2 nanowires at the cathode showed a charge storage capacity of 3000 mA h g$_{carbon}^{-1}$ (or 505 mA h g^{-1} if normalized by the total electrode mass).[127] Of a number of other metal oxide catalysts studied,[128] a high initial capacity was observed with Fe_2O_3, Fe_3O_4, CuO and $CoFe_2O_4$.[124,125] Au/C and Pt/C catalysts were shown to reduce the overpotentials of ORR or OER in a Li–O_2 battery, and a PtAu/C catalyst was shown to exhibit bifunctional catalytic activity in which the surface Au and Pt atoms responsible for ORR and OER kinetics, respectively.[127,128] A significant reduction of the charging voltage in a Li–O_2 cell was demonstrated using the AuPt/C catalyst for the oxygen cathode under the condition of a low discharging–charging current density (0.04 mA cm$_{electrode}^{-2}$).[127] In general, the understanding of the catalytic mechanisms of various catalysts in Li-oxygen batteries is complicated by electrolyte decomposition.[129,130] Many common solvents were shown to not be stable on cycling

in rechargeable Li–O$_2$batteries, which indicates an additional challenge in terms of identifying solvents resistant to attack by the reduced O$_2$ species. Recent exploration of the nanoalloy phase and composition of AuPt and other catalysts[131] has provided some useful insights into the control of structures of catalysts in rechargeable Li-air batteries.

To address the issue of the design of bifunctional catalysts in terms of nanoscale phase structures, Au$_m$Pt$_{100-m}$ nanoparticles were studied as a model system,[131] focusing on the effect of composition and phase characteristics of the AuPt catalysts on the overpotentials for both ORR and OER and the discharge–charge capacity. The phase-controllable catalysts were synthesized, and used as the cathode catalysts in a Li–O$_2$ cell for the measurement of the discharge–charge voltage difference and the discharge capacity. For the air cathode of a rechargeable Li-air battery which involves both ORR and OER, this feature is partially similar to the ORR at the cathode of a fuel cell, but the complication of the deposition of LiO$_2$ in ORR on the catalyst and the reoxidation of LiO$_2$ in OER poses a new challenge for the design of an effective catalyst. While different binary and ternary catalysts are being investigated, the recent insight obtained from the study of AuPt catalysts as air cathode catalyst serves as an excellent example to illustrate the catalytic properties. This study stems partly from our recent demonstration of bifunctional catalytic activity of catalysts of different compositions for ORR and MOR in fuel cell reactions in correlation with size, composition, alloying and phase segregation, focusing on the nanostructural effect on the catalytic characteristics.

The catalysts with fully-alloyed phases exhibits a smaller discharge–charge voltage difference and a higher discharge capacity than those with a partial phase segregation, demonstrating the importance of the control of the composition and phase properties of the gold-based alloy catalysts. The Au$_{49}$Pt$_{51}$/C catalyst in a solvent of 1 : 1 mixed ethylene carbonate and dimethyl carbonate under a current density of 0.12 mA cm^{-2} exhibits a discharge capacity of 1329 mA h g^{-1} carbon. With another solvent that is free of the carbonate structure, i.e., tetraethylene glycol dimethyl ether, the first discharge–charge cycle measured under 0.12 mA cm^{-2} shows a capacity of 1622 m A h g$_{carbon}^{-1}$. The second cycle measured under 0.06 mA cm^{-2} exhibits slightly lower capacity (1410 m A h g$_{carbon}^{-1}$), but there is a significant improvement in overpotential. A comparison of the redox characteristics between the catalysts of different bimetallic compositions suggests that AuPt catalyst enables the redox reaction to remain largely at the stage of superoxides between ORR and OER reactions in the organic electrolyte. The catalysts with fully-alloyed phases exhibits a smaller discharge–charge voltage difference and a higher discharge capacity than those with a partial phase segregation. The catalyst phase characteristics of the catalysts influence the overpotentials for both ORR and OER, demonstrating the viability of designing phase-controllable catalysts for manipulating the discharge–charge voltage difference and the discharge capacity of the Li–O$_2$ cell.[131]

Built upon the understanding of the nanoalloy's phase characteristics and recent understanding of electrolyte effects on the battery performance,[30,120,132] two important fronts of our

investigations include: the study of nanoalloy catalysts of selected binary and ternary compositions, and the study of electrolytes of different structures and properties. Studies of various catalysts or composite materials and different electrolytes have indicated that there is a clear need to seek not only a better electrolyte but also to design a better catalyst that can suppress the decomposition of the electrolyte. There is also clear need to assess the cycle life of the catalyst in the battery cell, as the discharge capacities have been found to decrease significantly upon multiple cycles. In addition to the problem associated with dendrite growth at the anode side, which is a concern for the long-term operation of rechargeable batteries using a Li metal anode, solvent decomposition is also a serious problem for the low cycle life.

4. Summary and perspectives

In summary, enhanced electrocatalytic activities for several reduction and oxidation reactions in fuel cells or Li-air batteries have been demonstrated by a combination of alloying platinum or palladium with other transition metals and nanoengineering the catalyst structures. It is the unique nanoscale phenomena in terms of atomic-scale alloying, interatomic distances, metal coordination structures, structural/chemical ordering, and phase states that operate synergistically in activating oxygen and maneuvering surface oxygenated species, providing important information for the design of catalysts with high activity at significantly-reduced use of noble metals. In addition to studies aimed at further lowering the noble metal content in the nanoalloy catalysts, future work is needed in the area of theoretical computation and modelling to understand how the structural-catalytic synergy are influenced by the binary or ternary metal composition. This understanding will also guide the development of the ability to control the stability of metal components in the nanoalloy catalysts under the electrocatalytic operation conditions. To aid this controllability, *in situ* experiments are needed to probe the structural evolution processes such as de-alloying process in the electrolyteand atomic-scale rearrangements leading to changes in size, shape, or surface energy. With the recent advents in applying synchrotron X-ray based techniques in various catalyst systems, in-depth understanding of nanoalloy design parameters for achieving high activity and high stability will further advance the endeavour of electrochemical energy conversion and storage.

Acknowledgements

References

1 J. B. Wu and H. Yang, *Acc. Chem. Res.*, 2013, **46**, 1848–1857.

2 A. K. Singh and Q. Xu, *ChemCatChem*, 2013, **5**, 652–676.

3 S. J. Guo, S. Zhang and S. H. Sun, *Angew. Chem., Int. Ed.*, 2013, **52**, 8526–8544.

4 N. V. Long, Y. Yang, C. M. Thi, N. V. Minh, Y. Q. Cao and M. Nogami, *Nano Energy*, 2013, **2**, 636–676.

5 R. Ferrando, J. Jellinek and R. L. Johnston, *Chem. Rev.*, 2008, **108**, 845–910.

6 H. A. Gasteiger, S. S. Kocha, B. Sompalli and F. T. Wagner, *Appl. Catal., B*, 2005, **56**, 9–35.

7 A. Brouzgou, S. Q. Song and P. Tsiakaras, *Appl. Catal., B*, 2012, **127**, 371–388.

8 C. Wang, N. M. Markovic and V. R. Stamenkovic, *ACS Catal.*, 2012, **2**, 891–898.

9 M. K. Jeon, C. H. Lee, G. I. Park and K. H. Kang, *J. Power Sources*, 2012, **216**, 400–408.

10 M. Watanabe, D. A. Tryk, M. Wakisaka, H. Yano and H. Uchida, *Electrochim. Acta*, 2012, **84**, 187–201.

11 C.-H. Cui and S.-H. Yu, *Acc. Chem. Res.*, 2013, **46**, 1427–1437.

12 J. L. Fernandez, D. A. Walsh and A. J. Bard, *J. Am. Chem. Soc.*, 2005, **127**, 357–365.

13 J. K. Nørskov, J. Rossmeisl, A. Logadottir, L. Lindqvist, J. R. Kitchin, T. Bligaard and H. Jonsson, *J. Phys. Chem. B*, 2004, **108**, 17886–17892.

14 N. P. Brandon, S. Skinner and B. C. H. Steele, *Annu. Rev. Mater. Res.*, 2003, **33**, 183–213.

15 S. B. Adler, *Chem. Rev.*, 2004, **104**, 4791–4843.

16 E. Casado-Rivera, D. J. Volpe, L. Alden, C. Lind, C. Downie, T. Vazquez-Alvarez, A. C. D. Angelo, F. J. Di Salvo and H. D. Abruna, *J. Am. Chem. Soc.*, 2004, **126**, 4043–4049.

17 K. Sasaki, J. X. Wang, M. Balasubramanian, J. McBreen, F. Uribe and R. R. Adzic, *Electrochim. Acta*, 2004, **49**, 3873–3877.

18 V. R. Stamenkovic, B. S. Mun, M. Arenz, K. J. J. Mayrhofer, C. A. Lucas, G. F. Wang, P. N. Ross and N. M. Markovic, *Nat. Mater.*, 2007, **6**, 241–247.

19 V. Stamenkovic, T. J. Schmidt, P. N. Ross and N. M. Markovic, *J. Electroanal. Chem.*, 2003, **554**, 191–199.

20 J. Zhang and C. M. Li, *Chem. Soc. Rev.*, 2012, **41**, 7016–7031.

21 J. Greeley, I. E. L. Stephens, A. S. Bondarenko, T. P. Johansson, H. A. Hansen, T. F. Jaramillo, J. Rossmeisl, I. Chorkendorff and J. K. Norskov, *Nat. Chem.*, 2009, **1**, 552–556.

22 V. R. Stamenkovic, B. Fowler, B. S. Mun, G. F. Wang, P. N. Ross, C. A. Lucas and N. M. Markovic, *Science*, 2007, **315**, 493–497.

23 V. Stamenkovic, T. J. Schmidt, P. N. Ross and N. M. Markovic, *J. Phys. Chem. B*, 2002, **106**, 11970–11979.

24 S. Mukerjee, S. Srinivasan, M. P. Soriaga and J. McBreen, *J. Electrochem. Soc.*, 1995, **142**, 1409–1422.

25 T. Toda, H. Igarashi, H. Uchida and M. Watanabe, *J. Electrochem. Soc.*, 1999, **146**, 3750–3756.

26 T. Toda, H. Igarashi and M. Watanabe, *J. Electroanal. Chem.*, 1999, **460**, 258–262.

27 A. K. Shukla and R. K. Raman, *Annu. Rev. Mater. Res.*, 2003, **33**, 155–168.

28 A. Kowal, M. Li, M. Shao, K. Sasaki, M. B. Vukmirovic, J. Zhang, N. S. Marinkovic, P. Liu, A. I. Frenkel and R. R. Adzic, *Nat. Mater.*, 2009, **8**, 325–330.

29 Q. G. He, B. Shyam, K. Macounova, P. Krtil, D. Ramaker and S. Mukerjee, *J. Am. Chem. Soc.*, 2012, **134**, 8655–8661.

30 Y. C. Lu, B. M. Gallant, D. G. Kwabi, J. R. Harding, R. R. Mitchell, M. S. Whittingham and Y. Shao-Horn, *Energy Environ. Sci.*, 2013, **6**, 750–768.

31 J. D. Aiken and R. G. Finke, *J. Mol. Catal. A: Chem.*, 1999, **145**, 1–44.

32 H. Li, Y. Y. Luk and M. Mrksich, *Langmuir*, 1999, **15**, 4957–4959.

33 C. J. Zhong and M. M. Maye, *Adv. Mater.*, 2001, **13**, 1507–1511.

34 X. G. Peng, M. C. Schlamp, A. V. Kadavanich and A. P. Alivisatos, *J. Am. Chem. Soc.*, 1997, **119**, 7019–7029.

35 T. H. Galow, U. Drechsler, J. A. Hanson and V. M. Rotello, *Chem. Commun.*, 2002, 1076–1077.

36 M. Brust, M. Walker, D. Bethell, D. J. Schiffrin and R. Whyman, *J. Chem. Soc., Chem. Commun.*, 1994, 801–802.

37 A. C. Templeton, M. P. Wuelfing and R. W. Murray, *Acc. Chem. Res.*, 2000, **33**, 27–36.

38 T. J. Schmidt, H. A. Gasteiger and R. J. Behm, *Electrochem. Commun.*, 1999, **1**, 1–4.

39 U. A. Paulus, U. Endruschat, G. J. Feldmeyer, T. J. Schmidt, H. Bonnemann and R. J. Behm, *J. Catal.*, 2000, **195**, 383–393.

40 R. L. Whetten, J. T. Khoury, M. M. Alvarez, S. Murthy, I. Vezmar, Z. L. Wang, P. W. Stephens, C. L. Cleveland, W. D. Luedtke and U. Landman, *Adv. Mater.*, 1996, **8**, 428–433.

41 M. A. El-Sayed, *Acc. Chem. Res.*, 2001, **34**, 257–264.

42 F. Caruso, *Adv. Mater.*, 2001, **13**, 11–22.

43 J. J. Storhoff and C. A. Mirkin, *Chem. Rev.*, 1999, **99**, 1849–1862.

44 S. H. Sun, C. B. Murray, D. Weller, L. Folks and A. Moser, *Science*, 2000, **287**, 1989–1992.

45 M. Chen and D. E. Nikles, *Nano Lett.*, 2002, **2**, 211–214.

46 Y. H. Zhang, Z. Y. Duan, C. Xiao and G. F. Wang, *Surf. Sci.*, 2011, **605**, 1577–1582.

47 L. F. Yang, S. Y. Shan, R. Loukrakpam, V. Petkov, Y. Ren, B. N. Wanjala, M. H. Engelhard, J. Luo, J. Yin, Y. S. Chen and C. J. Zhong, *J. Am. Chem. Soc.*, 2012, **134**, 15048–15060.

48 V. Petkov, B. N. Wanjala, R. Loukrakpam, J. Luo, L. F. Yang, C. J. Zhong and S. Shastri, *Nano Lett.*, 2012, **12**, 4289–4299.

49 B. N. Wanjala, B. Fang, S. Y. Shan, V. Petkov, P. Y. Zhu, R. Loukrakpam, Y. S. Chen, J. Luo, J. Yin, L. F. Yang, M. H. Shao and C. J. Zhong, *Chem. Mater.*, 2012, **24**, 4283–4293.

50 J. Yin, S. Y. Shan, L. F. Yang, D. Mott, O. Malis, V. Petkov, F. Cai, M. S. Ng, J. Luo, B. H. Chen, M. Engelhard and C. J. Zhong, *Chem. Mater.*, 2012, **24**, 4662–4674.

51 R. Loukrakpam, S. Y. Shan, V. Petkov, L. F. Yang, J. Luo and C. J. Zhong, *J. Phys. Chem. C*, 2013, **117**, 20715–20721.

52 V. Petkov, Y. Ren, S. Y. Shan, J. Luo and C. J. Zhong, *Nanoscale*, 2014, **6**, 532–538.

53 S. Y. Shan, V. Petkov, L. F. Yang, D. Mott, B. N. Wanjala, F. Cai, B. H. Chen, J. Luo and C. J. Zhong, *ACS Catal.*, 2013, **3**, 3075–3085.

54 N. N. Kariuki, J. Luo, L. Han, M. M. Maye, L. Moussa, M. Patterson, Y. H. Lin, M. H. Engelhard and C. J. Zhong, *Electroanalysis*, 2004, **16**, 120–126.

55 S. Nishimura, T. N. D. Anh, D. Mott, K. Ebitani and S. Maenosono, *J. Phys. Chem. C*, 2012, **116**, 4511–4516.

56 J. Yin, S. Y. Shan, M. S. Ng, L. F. Yang, D. Mott, W. Q. Fang, N. Kang, J. Luo and C. J. Zhong, *Langmuir*, 2013, **29**, 9249–9258.

57 K. J. Klabunde and R. S. Mulukutla, in *Nanoscale Materials in Chemistry*, ed. K. J. Klabunde, John Wiley & Sons, Inc., New York, 2001, p. 223.

58 U. A. Paulus, A. Wokaun, G. G. Scherer, T. J. Schmidt, V. Stamenkovic, V. Radmilovic, N. M. Markovic and P. N. Ross, *J. Phys. Chem. B*, 2002, **106**, 4181–4191.

59 E. Antolini, *Mater. Chem. Phys.*, 2003, **78**, 563–573.

60 H. Yang, W. Vogel, C. Lamy and N. Alonso-Vante, *J. Phys. Chem. B*, 2004, **108**, 11024–11034.

61 D. L. Feldheim and C. A. Foss Jr, in *Metal Nanoparticles: Synthesis, Characterization, and Applications*, Marcel Dekker, Inc., New York, 2002.

62 P. Waszczuk, G. Q. Lu, A. Wieckowski, C. Lu, C. Rice and R. I. Masel, *Electrochim. Acta*, 2002, **47**, 3637–3652.

63 T. J. Schmidt, H. A. Gasteiger and R. J. Behm, *Electrochem. Commun.*, 1999, **1**, 1–4.

64 R. Raja, T. Khimyak, J. M. Thomas, S. Hermans and B. F. G. Johnson, *Angew. Chem., Int. Ed.*, 2001, **40**, 4638–4642.

65 C. J. Zhong and J. R. Regalbuto, *Comprehensive Inorganic Chemistry II*, Elsevier, 2013, vol. 7, pp. 75–102.

66 L. C. Liu, X. R. Gu, Y. Cao, X. J. Yao, L. Zhang, C. J. Tang, F. Gao and L. Dong, *ACS Catal.*, 2013, **3**, 2768–2775.

67 X. Y. Liu, A. Q. Wang, T. Zhang and C. Y. Mou, *Nano Today*, 2013, **8**, 403–416.

68 M. Haruta, S. Tsubota, T. Kobayashi, H. Kageyama, M. J. Genet and B. Delmon, *J. Catal.*, 2003, **144**, 175–192.

69 J. Luo, P. N. Njoki, Y. Lin, L. Y. Wang and C. J. Zhong, *Electrochem. Commun.*, 2006, **8**, 581–587.

70 J. Luo, N. Kariuki, L. Han, L. Y. Wang, C. J. Zhong and T. He, *Electrochim. Acta*, 2006, **51**, 4821–4827.

71 L. Han, W. Wu, F. L. Kirk, J. Luo, M. M. Maye, N. N. Kariuki, Y. H. Lin, C. M. Wang and C. J. Zhong, *Langmuir*, 2004, **20**, 6019–6025.

72 B. N. Wanjala, B. Fang, R. Loukrakpam, Y. S. Chen, M. Engelhard, J. Luo, J. Yin, L. F. Yang, S. Y. Shan and C. J. Zhong, *ACS Catal.*, 2012, **2**, 795.

73 B. N. Wanjala, J. Luo, B. Fang, D. Mott and C. J. Zhong, *J. Mater. Chem.*, 2011, **21**, 4012–4020.

74 B. N. Wanjala, J. Luo, R. Loukrakpam, B. Fang, D. Mott, P. N. Njoki, M. Engelhard, H. R. Naslund, J. K. Wu, L. C. Wang, O. Malis and C. J. Zhong, *Chem. Mater.*, 2010, **22**, 4282–4294.

75 J. Evans, in *Catalysis*, ed. G. C. Bond and G. Webb, Royal Society of Chemistry, 1989, vol. 8, p. 1.

76 C. Antoniak, *Beilstein J. Nanotechnol.*, 2011, **2**, 237–251.

77 B. Wanjala, R. Loukrakpam, J. Luo, P. N. Njoki, D. Mott, M. Shao, L. Protsailo, T. Kawamura and C. J. Zhong, *J. Phys. Chem. C*, 2010, **114**, 17580–17590.

78 V. Petkov, S. Shastri, S. Shan, P. Joseph, J. Luo, C. J. Zhong, T. Nakamura, Y. Herbani and S. Sato, *J. Phys. Chem. C*, 2013, **117**, 22131–22141.

79 R. Loukrakpam, B. N. Wanjala, J. Yin, B. Fang, J. Luo, M. Shao, L. Protsailo, T. Kawamura, Y. Chen, V. Petkov and C. J. Zhong, *ACS Catal.*, 2011, **1**, 562–572.

80 R. Loukrakpam, J. Luo, T. He, Y. Chen, Z. Xu, P. N. Njoki, B. N. Wanjala, B. Fang, D. Mott, J. Yin, J. Klar, B. Powell and C. J. Zhong, *J. Phys. Chem. C*, 2011, **115**, 1682–1694.

81 L. Wang, J. I. Williams, T. Lin and C. J. Zhong, *Catal. Today*, 2011, **165**, 150–159.

82 M. J. Schadt, W. Cheung, J. Luo and C. J. Zhong, *Chem. Mater.*, 2006, **18**, 5147–5149.

83 D. Mott, J. Luo, P. N. Njoki, Y. Lin, L. Y. Wang and C. J. Zhong, *Catal. Today*, 2007, **122**, 378–385.

84 B. H. Morrow and A. Striolo, *Phys. Rev. B: Condens. Matter Mater. Phys.*, 2010, **81**, 155437.

85 J. Luo, L. Wang, D. Mott, P. N. Njoki, Y. Lin, T. He, Z. Xu, B. N. Wanjana, I. I. S. Lim and C. J. Zhong, *Adv. Mater.*, 2008, **20**, 4342–4347.

86 O. Malis, M. Radu, D. Mott, B. Wanjala, J. Luo and C. J. Zhong, *Nanotechnology*, 2009, **20**, 245705–245708.

87 G. Kresse and J. Hafner, *Phys. Rev. B: Condens. Matter Mater. Phys.*, 1993, **47**, 558–561.

88 G. Kresse and J. Furthmuller, *Phys. Rev. B: Condens. Matter Mater. Phys.*, 1996, **54**, 11169–11186.

89 G. Kresse and J. Furthmuller, *Comput. Mater. Sci.*, 1996, **6**, 15–50.

90 J. Luo, M. M. Maye, V. Petkov, N. N. Kariuki, L. Y. Wang, P. Njoki, D. Mott, Y. Lin and C. J. Zhong, *Chem. Mater.*, 2005, **17**, 3086–3091.

91 D. Bochicchio, F. Negro and R. Ferrando, *Comput. Theor. Chem.*, 2013, **1021**, 177–182.

92 K. Suarez-Alcantara, A. Rodriguez-Castellanos, R. Dante and O. Solorza-Feria, *J. Power Sources*, 2006, **157**, 114–120.

93 C. J. Zhong, J. Luo, B. Fang, B. Wanjala, P. Njoki, R. Loukrakpam and J. Yin, *Nanotechnology*, 2010, **21**, 061992–062001.

94 C. Wang, M. Chi, D. Li, D. Strmcnik, D. van der Vliet, G. Wang, V. Komanicky, K.-C. Chang, A. P. Paulikas, D. Tripkovic, J. Pearson, K. L. More, N. M. Markovic and V. R. Stamenkovic, *J. Am. Chem. Soc.*, 2011, **133**, 14396–14403.

95 C. Wang, D. van der Vliet, K.-C. Chang, H. You, D. Strmcnik, J. A. Schlueter, N. M. Markovic and V. R. Stamenkovic, *J. Phys. Chem. C*, 2009, **113**, 19365–19368.

96 D. van der Vliet, D. S. Strmcnik, C. Wang, V. R. Stamenkovic, N. M. Markovic and M. T. M. Koper, *J. Electroanal. Chem.*, 2010, **647**, 29–34.

97 B. Wanjala, B. Fang, J. Luo, Y. Chen, J. Yin, M. Engelhard, R. Loukrakpam and C. J. Zhong, *J. Am. Chem. Soc.*, 2011, **133**, 12714–12727.

98 S. D. Senanayake, D. Stacchiola and J. A. Rodriguez, *Acc. Chem. Res.*, 2013, **46**, 1702–1711.

99 C. J. Zhong, J. Luo, P. N. Njoki, D. Mott, B. Wanjala, R. Loukrakpam, S. Lim, L. Wang, B. Fang and Z. C. Xu, *Energy Environ. Sci.*, 2008, **1**, 454–466.

100 M. Subhramannia and V. K. Pillai, *J. Mater. Chem.*, 2008, **18**, 5858–5870.

101 J. T. Miller, A. J. Kropf, Y. Zha, J. R. Regalbuto, L. Delannoy, C. Louis, E. Bus and J. A. van Bokhoven, *J. Catal.*, 2006, **240**, 222–234.

102 J. H. Kang, L. D. Menard, R. G. Nuzzo and A. I. Frenkel, *J. Am. Chem. Soc.*, 2006, **128**, 12068–12069.

103 S. Mukerjee, S. Srinivasan, M. P. Soriaga and J. Mcbreen, *J. Electrochem. Soc.*, 1995, **142**, 1409–1422.

104 T. S. Chou, M. L. Perlman and R. E. Watson, *Phys. Rev. B: Solid State*, 1976, **14**, 3248–3250.

105 T. Rajasekharan and V. Seshubai, *Acta Crystallogr., Sect. A: Found. Crystallogr.*, 2012, **68**, 156–165.

106 K. Tedsree, C. W. A. Chan, S. Jones, Q. A. Cuan, W. K. Li, X. Q. Gong and S. C. E. Tsang, *Science*, 2011, **332**, 224–228.

107 C. Berg, H. J. Venvik, F. Strisland, A. Ramstad and A. Borg, *Surf. Sci.*, 1998, **409**, 1–15.

108 Q. Ge, C. Song and L. Wang, *Comput. Mater. Sci.*, 2006, **35**, 247–253.

109 S. Galvagno and G. Parravano, *J. Catal.*, 1979, **57**, 272–286.

110 G. Selvarani, S. V. Selvaganesh, S. Krishnamurthy, G. V. M. Kiruthika, P. Sridhar, S. Pitchumani and A. K. Shukla, *J. Phys. Chem. C*, 2009, **113**, 7461–7468.

111 D. Dai and K. Balasubramanian, *J. Chem. Phys.*, 1994, **100**, 4401–4407.

112 W. Q. Tian, M. F. Ge, F. L. Gu, T. Yamada and Y. Aoki, *J. Phys. Chem. A*, 2006, **110**, 6285–6293.

113 M. O. Pedersen, S. Helveg, A. Ruban, I. Stensgaard, E. Laegsgaard, J. K. Norskov and F. Besenbacher, *Surf. Sci.*, 1999, **426**, 395–409.

114 E. Skulason, V. Tripkovic, M. E. Bjorketun, S. Gudmundsdottir, G. Karlberg, J. Rossmeisl, T. Bligaard, H. Jonsson and J. K. Norskov, *J. Phys. Chem. C*, 2010, **114**, 18182–18197.

115 W. J. Zhou, B. Zhou, W. Z. Li, Z. H. Zhou, S. Q. Song, G. Q. Sun, Q. Xin, S. Douvartzides, A. Goula and P. Tsiakaras, *J. Power Sources*, 2004, **126**, 16–22.

116 K. Tadanaga, Y. Furukawa, A. Hayashi and M. Tatsumisago, *Adv. Mater.*, 2010, **22**, 4401–4404.

117 M. M. Dimos and G. J. Blanchard, *J. Phys. Chem. C*, 2010, **114**, 6019–6026.

118 Z. X. Liang, T. S. Zhao, J. B. Xu and L. D. Zhu, *Electrochim. Acta*, 2009, **54**, 2203–2208.

119 J. Yin, J. Luo, B. Wanjala, B. Fang, R. Loukrakpam and C. J. Zhong, *New and Future Developments in Catalysis: Batteries, Hydrogen Storage and Fuel Cells*, ed. S. L. Suib, Elsevier, 2013, ch. 11, pp. 307–344.

120 J. Lu and K. Amine, *Energies*, 2013, **6**, 6016–6044.

121 K. M. Abraham, *ECS Trans.*, 2008, **3**, 67–71.

122 W. Xu, J. Xiao, D. Wang, J. Zhang and J. G. Zhang, *J. Electrochem. Soc.*, 2010, **157**, A219–A244.

123 T. Ogasawara, A. Debart, M. Holzapfel, P. Novak and P. G. Bruce, *J. Am. Chem. Soc.*, 2006, **128**, 1390–1393.

124 A. Debart, A. J. Paterson, J. Bao and P. G. Bruce, *Angew. Chem., Int. Ed.*, 2008, **47**, 4521–4524.

125 A. Debart, J. Bao, G. Armstrong and P. G. Bruce, *J. Power Sources*, 2007, **174**, 1177–1182.

126 Z. Peng, S. A. Freunberger, Y. Chen and P. G. Bruce, *Science*, 2012, **337**, 563–566.

127 Y. C. Lu, Z. Xu, H. A. Gasteiger, S. Chen, K. Hamad-Schifferli and Y. Shao-Horn, *J. Am. Chem. Soc.*, 2010, **132**, 12170–12171.

128 Y. C. Lu, H. A. Gasteiger, E. Crumlin, R. McGuire and Y. Shao-Horn Jr, *J. Electrochem. Soc.*, 2010, **157**, A1016–A1025.

129 S. A. Freunberger, Y. Chen, Z. Peng, J. M. Griffin, L. J. Hardwick, F. Barde, P. Novak and P. G. Bruce, *J. Am. Chem. Soc.*, 2011, **133**, 8040–8047.

130 Y.-C. Lu, D. G. Kwabi, K. P. C. Yao, J. R. Harding, J. Zhou, L. Zuin and Y. Shao-Horn, *Energy Environ. Sci.*, 2011, **4**, 2999–3007.

131 J. Yin, B. Fang, J. Luo, B. Wanjala, D. Mott, R. Loukrakpam, M. S. Ng, Z. Li, J. Hong, M. S. Whittingham and C. J. Zhong, *Nanotechnology*, 2012, **23**, 305404.

132 Z. Q. Peng, S. A. Freunberger, Y. H. Chen and P. G. Bruce, *Science*, 2012, **337**, 563–566.